ACS Photonics

pubs.acs.org/journal/apchd5

Article

Monolithic Barium Titanate Modulators on Silicon-on-Insulator Substrates

Zuoming Dong, Amogh Raju, Agham B. Posadas, Marc Reynaud, Alexander A. Demkov, and Daniel M. Wasserman*

Cite This: https://doi.org/10.1021/acsphotonics.3c01144

Read Online

ACCESS | Metrics & More | Article Recommendations | Supporting Information

ABSTRACT: The linear electro-optic (Pockels) effect provides a mechanism for the rapid (and ideally lossless) modulation of a material's refractive index. Barium titanate (BTO), a complex oxide with a large Pockels coefficient and low optical loss, is thus of significant interest for devices essential to integrated silicon photonics (modulators, phased arrays, tunable resonators), offering decreased operating voltages and/or footprints, low-loss operation, and compatibility with existing CMOS fabrication infrastructure. However, fabrication and growth challenges have limited the direct integration of monolithic BTO-based optoelectrics on silicon substrates. Here we demonstrate a low loss, monolithic BTO device architecture fabricated in thin film epitaxial BTO integrated on silicon-on-insulator substrates by using off-axis RF-sputtering. Mach−Zehnder interferometer modulators are fabricated in the as-grown BTO and characterized spectrally and as a function of DC and AC applied biases. The electro-optical modulators show low losses and competitive $V_\pi L$ values compared to state-of-the-art lithium niobate modulators, in a monolithic architecture compatible with CMOS electronics and silicon integrated photonic circuitry.

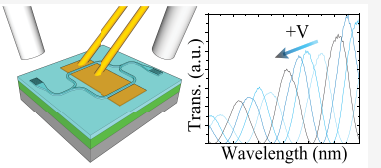

Monolithic BTO MZI Interferometer.

KEYWORDS: *barium titanate, silicon photonics, integrated photonics, Pockels effect, low loss waveguides, Mach−Zehnder interferometer*

INTRODUCTION

The class of materials generally termed complex oxides is becoming increasingly important for on-chip photonic integrated circuits (PICs). A key requirement for most integrated photonic systems is the ability to control the phase of propagating optical modes, a capability that can then be integrated into a variety of optoelectronic device architectures, such as modulators, phased-array emitters, and even optical frequency combs.[1−9] The most commonly used mechanisms to control the optical phase leverage either the thermo-optic effect (the change of refractive index with temperature)[10−12] or the plasma effect (the change of refractive index with carrier concentration).[13−15] Both approaches have been utilized to demonstrate a range of optical functionalities, but suffer from bandwidth limitations (thermo-optic) and/or increased loss (plasma effect).[1,16] There has thus been significant interest in mechanisms for the near-instantaneous control of the refractive index using optical nonlinearities, particularly the electro-optic effect, where the refractive index of a material can be tuned by the application of an electric field. Of particular interest is the linear electro-optic, or Pockels, effect, in which the refractive index of the electro-optic material varies linearly with the applied electric field. Leveraging this nonlinear (NL) response, bias-dependent changes to the real part (controlling phase), but not the imaginary part (responsible for loss), of the material's complex refractive index can be achieved.[17]

Over the past decade lithium niobate (LN) has emerged as such a material, with low optical loss[2,3,18−20] and a large Pockels coefficient (r_{33} = 31.45 pm/V, r_{42} = 33.96 pm/V[21]), ideal for a broad variety of optoelectronic devices and applications.[2,22−25] The success of LN as an optoelectronic material is in large part a result of its large Pockels coefficient, allowing for higher efficiency phase modulation (i.e., lower voltage) and/or smaller footprint electo-optic devices. The large Pockels coefficient of LN has enabled Mach−Zehnder interferometer (MZI) modulators of millimeter-scale lengths (3 mm,[26] 5 mm[20,26,27]). LN MZI's have been demonstrated with π phase-shifts at voltage-length products of $V_\pi L \approx 2.2$ V·cm[26] (using a base capacitor configuration) and $V_\pi L \approx 0.64$ V·cm[28,29] (using a carefully engineered top capacitor architecture). However, such devices are still quite large compared to typical CMOS electronic or even typical photonic device architectures. In addition, and perhaps, as importantly, lithium-containing materials are incompatible with CMOS fabrication processes, and for this reason, LN-based device integration with silicon substrates typically leverages wafer bonding

Received: August 16, 2023
Revised: November 9, 2023
Accepted: November 9, 2023

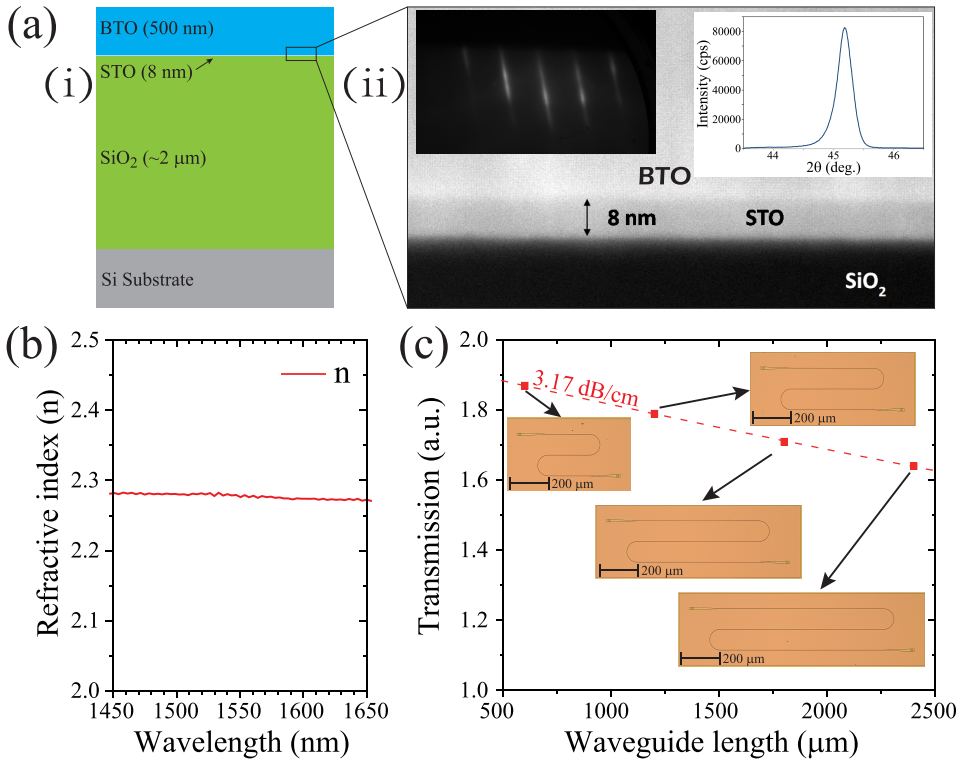

Figure 1. (a-i) Basic layer stack of RF-sputtered as-grown crystal-on-glass 500 nm thick BTO film. (a-ii) Background shows a representative transmission electron micrograph of RF-sputtered BTO grown on MBE-grown STO, itself grown on a SiO_2-on-Si substrate. Shown as insets are (left) a RHEED pattern and (right) an X-ray diffraction spectra of RF-sputtered BTO film, each indicating high quality crystal growth. (b) Extracted refractive index from ellipsometry measurements on the as-grown BTO material. (c) Experimental transmission through grating-coupled waveguides of varying lengths from which can be extracted a waveguide loss of 3.17 dB/cm. Inset images show the fabricated varying-length waveguides.

processes,[30] which can increase fabrication cost and complexity, and decrease device yield.

Barium titanate ($BaTiO_3$, or BTO) is one of the few materials which boasts a Pockels coefficient larger than that of LN, with measured thin-film and bulk electro-optic coefficients $r_{42\text{-BTO}}$ = 923 pm/V[31] and $r_{42\text{-BTO}}$ > 1000 pm/V,[32,33] respectively. Compared to LN ($r_{42\text{-LN}} \approx$ 34 pm/V), BTO thus offers a potentially significant decrease in device size (or operational voltage),[29] with practical implications for device packing density and/or power dissipation, as well as cost. BTO can be deposited on Si via molecular beam epitaxy (MBE), pulsed laser deposition, metal organic chemical vapor deposition, and RF-sputtering techniques,[34−36] and importantly, is compatible with the existing CMOS fabrication infrastructure. While BTO-based optoelectronic device development is in its early stages, there have been a number of demonstrations of devices leveraging BTO's large electro-optic coefficient. Many such demonstrations used BTO deposited on MgO[37−39] or lanthanum aluminate (LAO) substrates,[40] approaches that would still require heterogeneous integration with Si electronic or photonic devices.[31,41−43] In addition, patterning and etching of BTO are not yet well developed, and for this reason, many BTO-based photonic structures leverage a hybrid ridge waveguide architecture, where a deposited and patterned high index material serves to guide and confine the optical mode. Such an approach has resulted in remarkable performance,[29,31,39,41,42,44,45] with $V_\pi L$ as low as ∼0.23 V cm reported.[35,43,46] However, hybrid geometries have decreased overlap of the optical mode with the nonlinear BTO, and thus decreased the modulation efficiency ($V_\pi L$). The development of monolithic BTO-based optoelectronic devices, all else being equal, offers potential gains in device efficiency and decreased fabrication complexity. Comparison and discussion of the state-of-the-art in silicon photonics modulators, including LN and BTO (but also SiGe, SiGe/Si quantum wells, III−V materials leveraging the Franz-Keldysh effect and quantum confined Stark effect, lead zirconate titanate, and organic and 2D electro-optic materials) can be found in recent reviews which offer a comprehensive picture of the wide range of materials and device architectures currently employed and under investigation.[17,47]

In this work, we propose and demonstrate a monolithic BTO Mach−Zehnder interferometer leveraging low-loss all-BTO waveguides, ensuring nearly perfect overlap of the optical mode with the nonlinear material. The waveguides are fabricated from 500 nm-thick RF-sputtered BTO grown on a silicon-on-insulator (SOI) substrate.[35] RF-sputtered BTO offers high-quality epitaxial growth, and importantly, faster growth rates than MBE-grown BTO,[48] important for scalable, high-throughput production of the wavelength-scale thickness material requried for monolithic BTO optoelectronic device architectures.[35] The as-grown material is characterized, structurally and optically, the results of which are integrated into the MZI design. We design MZI devices with input/output couplers, tapers, y-splitters, bends, and straight waveguides for the telecom C-band $\lambda_o \approx$ 1535−1565 nm. The MZIs are fabricated using e-beam lithography (EBL) and ion-milling, and waveguide loss is measured using the cut-back method. We characterize the spectral behavior of the fabricated MZI modulators across the C-band, and measure the bias

https://doi.org/10.1021/acsphotonics.3c01144
ACS Photonics XXXX, XXX, XXX−XXX

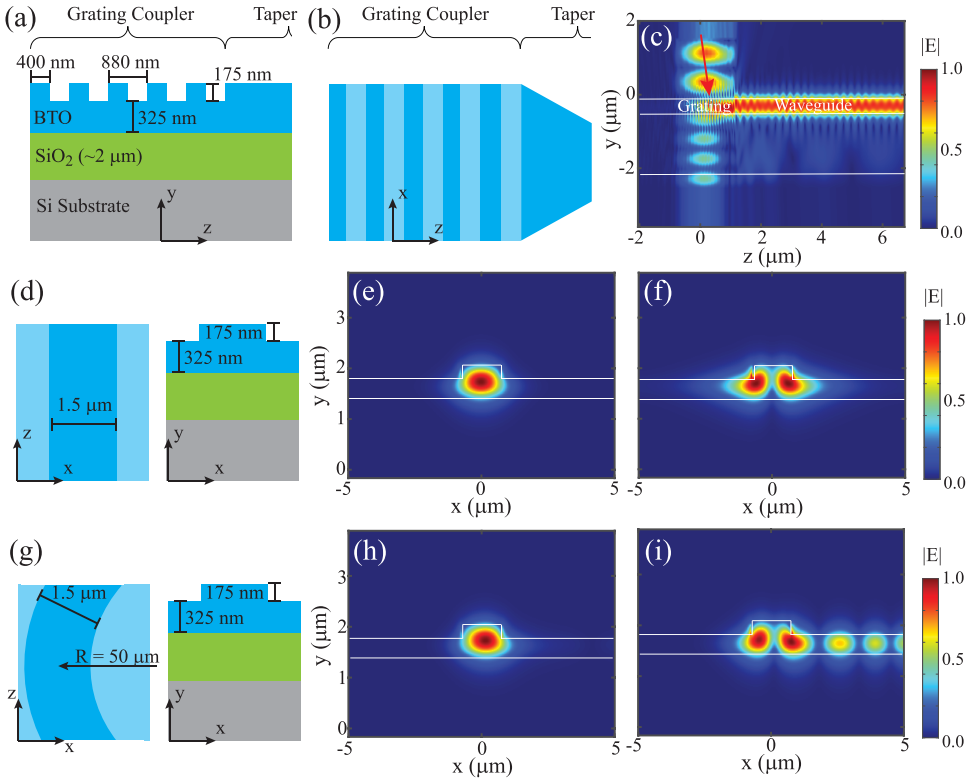

Figure 2. (a) Cross-sectional (*yz*) and (b) plan-view (*xz*) schematics of waveguide grating coupler. (c) Simulated cross-sectional (*yz*) field profile of λ_o = 1550 nm light incident at 8° from normal onto grating coupler. Note the multimode field profile for light in the waveguide portion of the simulation. (d) Plan view (*xz*) and cross-section (*xy*) of straight waveguide with cross-sectional (*xy*) field profiles of the (e) fundamental and (f) second-order TE modes. (g) Plan view (*xz*) and cross-section (*xy*) of bending (R = 50 μm) waveguide with cross-sectional (*xy*) field profiles of the (h) fundamental and (i) second-order TE modes. Note the significant leakage of the higher order mode.

dependent transmission of the interferometer as a function of applied DC bias. We also characterize response of the fabricated MZI to AC modulation for a range of DC biases. We extract a $V_\pi L$ = 2.32 V·cm, competitive with state-of-the-art LN modulators, and from this, an effective linear electro-optic coefficient of r_{eff} = 89 pm/V. These results are a promising step toward a CMOS compatible, monolithic electro-optic device architecture leveraging epitaxial sputtered BTO on Si (SOI) substrates.

METHODS

Growth. The BTO heterostructure was grown on a standard Soitec photonic silicon-on-insulator (SOI) wafer. The wafer was diced into ≈30 mm × 40 mm rectangles and degreased using sonication in acetone and isopropanol for 5 min each, followed by a 15 min exposure to UV/ozone. After outgassing, a 5 nm $SrTiO_3$ (STO) buffer was first grown by MBE after removing the native silicon oxide using Sr-assisted deoxidation and depositing one-half monolayer of Sr metal. The STO buffer was then grown in two steps: a 2 nm seed layer grown at 200 °C and crystallized at 550 °C, followed by an additional 3 nm of STO growth at 550 °C and 5 × 10^{-7} Torr of molecular oxygen. After the STO deposition, a patented controlled subsurface oxidation of the device Si layer is performed to transform the Si into SiO_2, which merges with the buried oxide layer of the SOI wafer without disrupting the overlying STO layer (crystal-on-glass technology[49]). The BTO was then grown by off-axis RF sputtering from a stoichiometric ceramic target in a sputter deposition chamber connected via an ultra high vacuum (UHV) buffer to the MBE growth chamber.[35] The target was presputtered for 10 min prior to deposition, which was done at 2.2 W/cm^2 power density, 10 mTorr total pressure with gas mixture of 30% O_2 and 70% Ar. The BTO was grown at 710 °C for a total time of 250 min. From prior calibration runs, this is expected to produce 500 nm of BTO. The sample is then cooled to room temperature at 10 °C/min before unloading from the UHV deposition system.

The as-grown sample has a layered structure shown in Figure 1a-i, with high-quality single-crystal BTO as evidenced by the transmission electron micrograph, reflection high energy electron diffraction (RHEED) pattern, and X-ray diffraction (XRD) spectra, as can be seen in Figure 1a-ii. Ellipsometry measurements of the as-grown BTO were taken, and the resulting data were fitted to extract the refractive index of the BTO (Figure 1b). From this, we estimated the BTO layer's refractive index to be n = 2.278 (with minimal loss, $\kappa \approx 0$) at a design wavelength of 1550 nm, approximating the BTO refractive index as isotropic.[29] Because the BTO loss, as measured by ellipsometry, was below the uncertainty of the measurement system, we designed and fabricated four waveguide structures of varying lengths, but with an equal number of bends and with the same grating couplers, and used the "cut-back" method to extract the waveguide loss of our monolithic BTO waveguides, shown in Figure 1c. While such an approach cannot extract the material loss of the BTO, it can provide a more practical measure of the loss associated with the waveguides in our monolithic BTO device architectures.

Design and Simulation. The refractive index extracted from the ellipsometry measurements of the as-grown BTO was used to design the optical components of the MZI. Figure 2

https://doi.org/10.1021/acsphotonics.3c01144
ACS Photonics XXXX, XXX, XXX−XXX

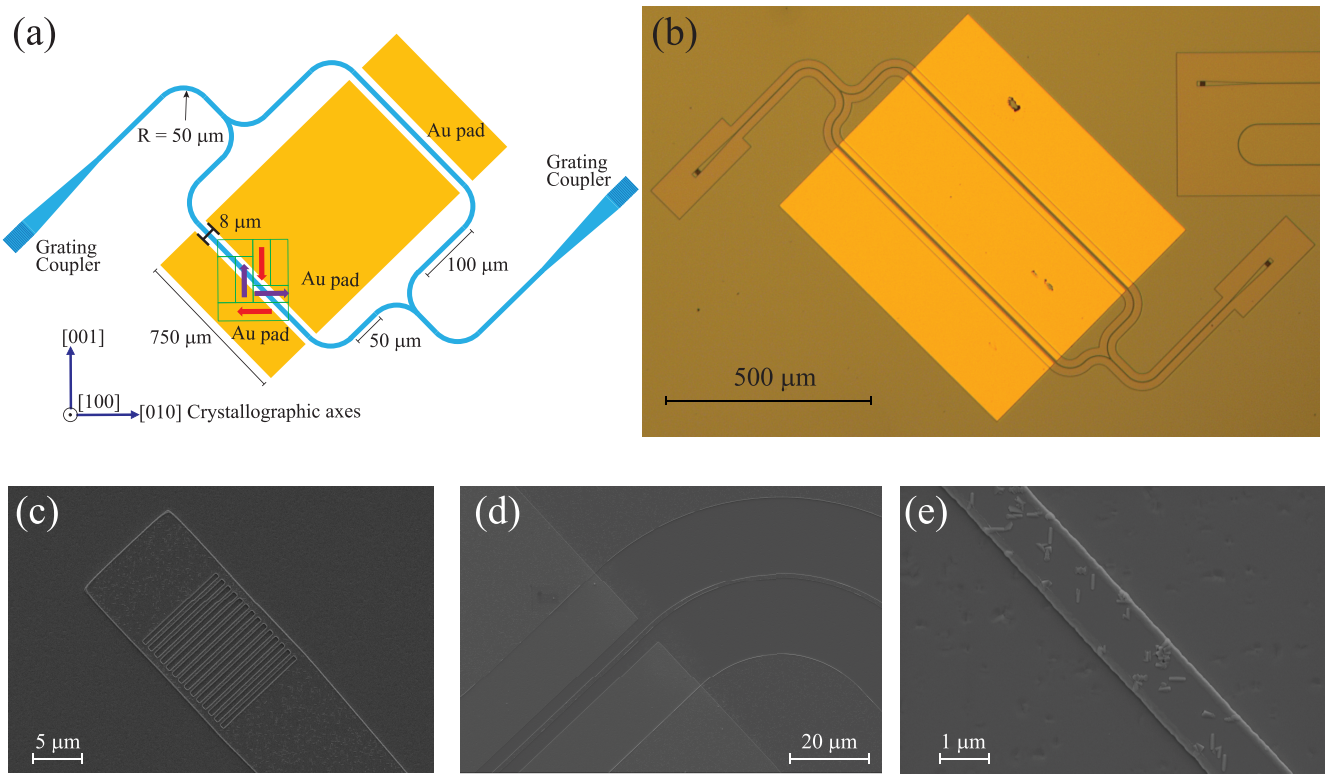

Figure 3. (a) Schematic of BTO Mach–Zehnder interferometer with 750 μm arm lengths. The BTO domain orientations are overlaid on the short arm of the MZI. (b) Optical micrograph of the fabricated BTO MZI. Scanning electron micrographs of the (c) grating coupler, (d) waveguide bend, straight arm, and Cr/Au electrodes, and (e) the straight waveguide section of the fabricated MZI.

shows the simulated performance of the key MZI components at λ_o = 1550 nm. The optical mode profiles and grating coupler efficiency were simulated using commercial finite difference time domain (FDTD) software (Lumerical). A 1D grating coupler model was used to calculate grating coupler efficiency (fraction of incident power coupled into the BTO waveguide). In order to simplify the device fabrication process, we assume that the grating and waveguide etch will be done simultaneously, which couples the waveguide ridge height and grating etch depth. We optimize etch depth across values which can be achieved using a single patterned e-beam resist mask, and determined this co-optimized etch depth to be 175 nm. The grating couplers are designed to in-couple and out-couple λ_o = 1550 nm light at angles of 8° from normal incidence. The optimized grating coupler geometry, for the fixed grating height and coupling angle, was determined to have a grating period of Λ = 880 nm with a grating ridge width of 400 nm. This grating coupler geometry results in a simulated grating coupling efficiency of 22%, which is adequate for characterizing the MZI performance. The field plot of incident light coupling into the BTO waveguide via the grating coupler is shown in Figure 2c. The excited mode profile in the waveguide section of the simulated system of Figure 2c shows some beating behavior, suggesting that incident light is coupled to both the fundamental and the higher order TE modes in the BTO waveguide.

To reduce scattering loss caused by sidewall roughness, we used a multimode waveguide design with waveguide width w = 1.5 μm. Waveguide mode simulations were performed with a 2D cross-section model, and the fundamental and second-order TE modes were simulated in both the straight waveguide (Figure 2d,e) and a waveguide with R = 50 μm bend radius (Figure 2g–i). The field plot of the bending waveguide clearly shows significant mode leakage for the second-order TE mode, but not for the fundamental mode. Thus, while the simulations suggest that some incident light will couple into the waveguide's second-order TE mode, the bends in the waveguide effectively filter this light, and therefore, the outcoupled (and thus modulated) signal is almost entirely the first-order TE waveguide mode.

Fabrication. The MZI device was fabricated from the as-grown BTO-on-SiO_2 layer stack shown in Figure 1a-i. Waveguides, tapers, and grating couplers were patterned by e-beam lithography (EBL) on a Raith system using an undiluted zep520a e-beam resist. The e-beam resist serves as an etch mask for the formation of the BTO waveguides and grating couplers. The BTO was etched by ion milling, using an AJA ion mill with a DC ion source of Ar^+ ions. The ion milling process was calibrated to obtain an etch rate of 8.6 nm/min and sidewall angle of about 75°. Following the waveguide/grating definition, the resist residue was cleaned from the sample surface. Electrodes were then pattered by using PMMA-A4 in a second EBL process. Metal contacts (Cr/Au, 6 nm/90 nm) are then deposited using a CHA e-beam evaporator system, and lift-off is performed in an acetone bath. The metal electrodes are patterned along the straight arms of the MZI with g = 8 μm gaps, with the waveguides centered between, and aligned to, the 750 μm long electrodes in the straight-waveguide portions of the MZI arms. Simulations of waveguide mode profiles, waveguide loss, and modal indices were performed for waveguides between electrodes of varying gap sizes. The gap size of g = 8 μm used in this work was determined to have no appreciable effect on waveguide loss or index, ensuring minimal reflection at the inputs to, and loss

https://doi.org/10.1021/acsphotonics.3c01144
ACS Photonics XXXX, XXX, XXX–XXX

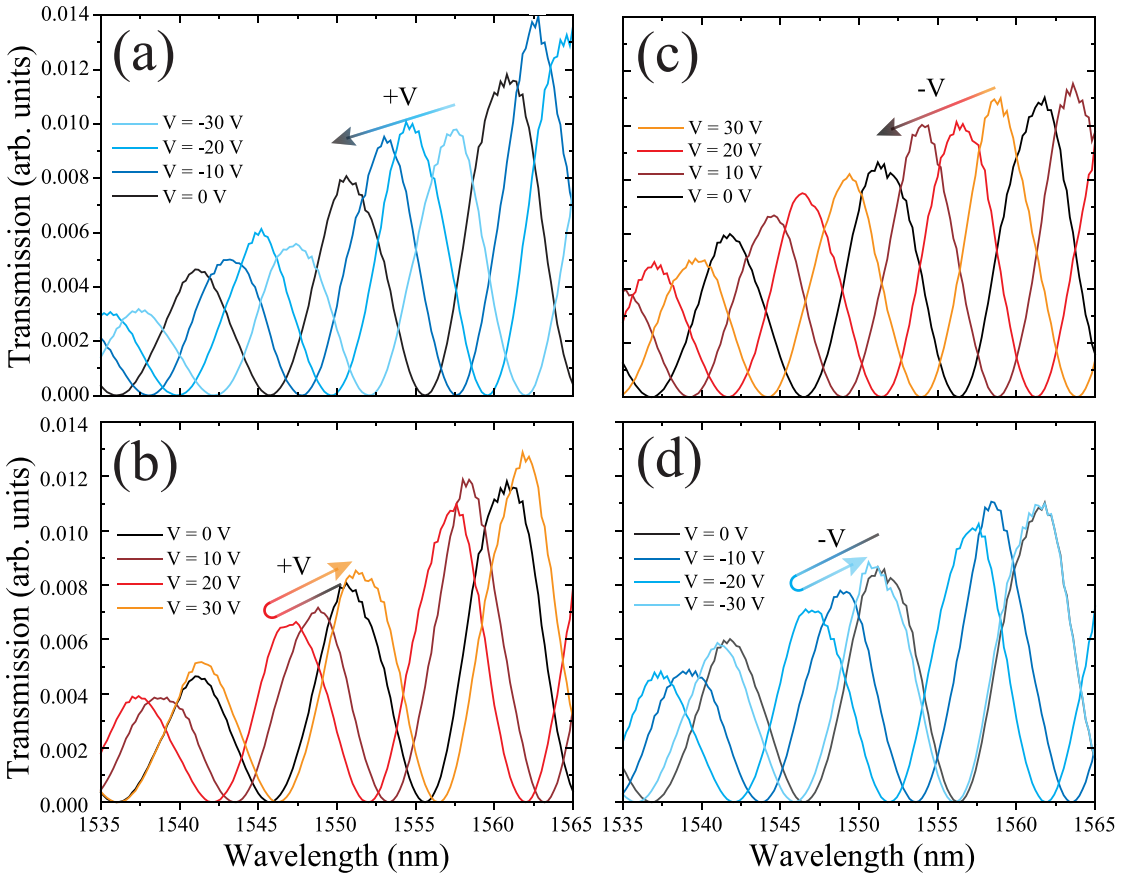

Figure 4. Transmission spectra of the MZI poled at −40 V for 60 min for DC biases from (a) −30 to 0 V and (b) 0 to 30 V, in 10 V increments. Transmission spectra of the MZI poled at 40 V for 60 min for DC biases from (c) 30 to 0 V and (d) 0 V to −30 V, in −10 V increments.

within, the biased arms of the MZI (Supporting Information, section 4). For compatibility with CMOS fabrication processes, the Au contacts would need to be replaced with an alternative metal; however, the choice of metal in this work has no effect on the device electrical or optical properties, and thus would not change the results presented here.

Figure 3a shows the schematic of the MZI with the 4 different possible BTO domain polarizations shown overlaying the lower arm of the MZI. The waveguide arms of the MZI are positioned parallel to the [01$\bar{1}$] direction of the BTO crystal such that the applied external fields are along the [011] direction of the BTO crystal. This ensures that all four domain variants are poled by the external field and thus contribute to electro-optical modulation.[50] Note also that the MZI is "unbalanced"; one arm is 100 μm longer than the other. This ensures a relative difference in phase accumulation in the two arms of the MZI, which will result in an oscillation between destructive and constructive interferences at the MZI output as the wavelength of the signal laser is varied. The spectral spacing in these interference fringes allows for the extraction of the group index (n_g) of the optical mode in the waveguides. Moreover, the unbalanced MZI also allows for AC modulation at quadrature points for any DC bias (including V_{DC} = 0 V), simply by adjusting the wavelength of the signal laser, which is something that would not be possible with a balanced MZI. Figure 3b shows an optical micrograph of the fabricated MZI, with contact pads, and Figures 3c−e show scanning electron micrographs of various components of the fabricated device: coupling gratings, waveguide bend and MZI arm, and straight waveguide, respectively. The ion-milled surfaces are notably smooth and uniform, while the unetched BTO shows some nanoscale features, remnants of the RF-sputtering growth process.

Electro-Optical Characterization. We first measure the transmission through the four waveguides of varying lengths, shown in the inset to Figure 1c. Because each of these waveguides is designed and fabricated to have the same grating coupler structures and the same number of (R = 50 μm) bends, the only difference in transmission efficiency should be the length of the straight waveguide components of the structures. Fitting the measured transmission to the relative lengths of the four waveguides (Figure 1c) allows for the extraction of an approximate waveguide loss, which we find to be 3.17 dB/cm. While the cut-back method employed here can suffer from waveguide-to-waveguide variation in coupling efficiency and fabrication defects, the excellent agreement between our single exponential fit and the measured transmission suggests minimal fabrication- or experiment-related variation between waveguides. The measured loss of our waveguides, before poling, is well below the state of the art for hybrid BTO waveguide structures,[43] and indicates the opportunity for low-loss, monolithic, BTO integrated photonic architectures.

Light from a fiber-coupled, tunable laser operating at λ_o = 1535−1565 nm is coupled into the MZI via the grating coupler and adiabatic waveguide taper. The polarization of the incident light was defined through a fiber polarization controller and adjusted to ensure TE-polarized incident light upon the in-

https://doi.org/10.1021/acsphotonics.3c01144
ACS Photonics XXXX, XXX, XXX−XXX

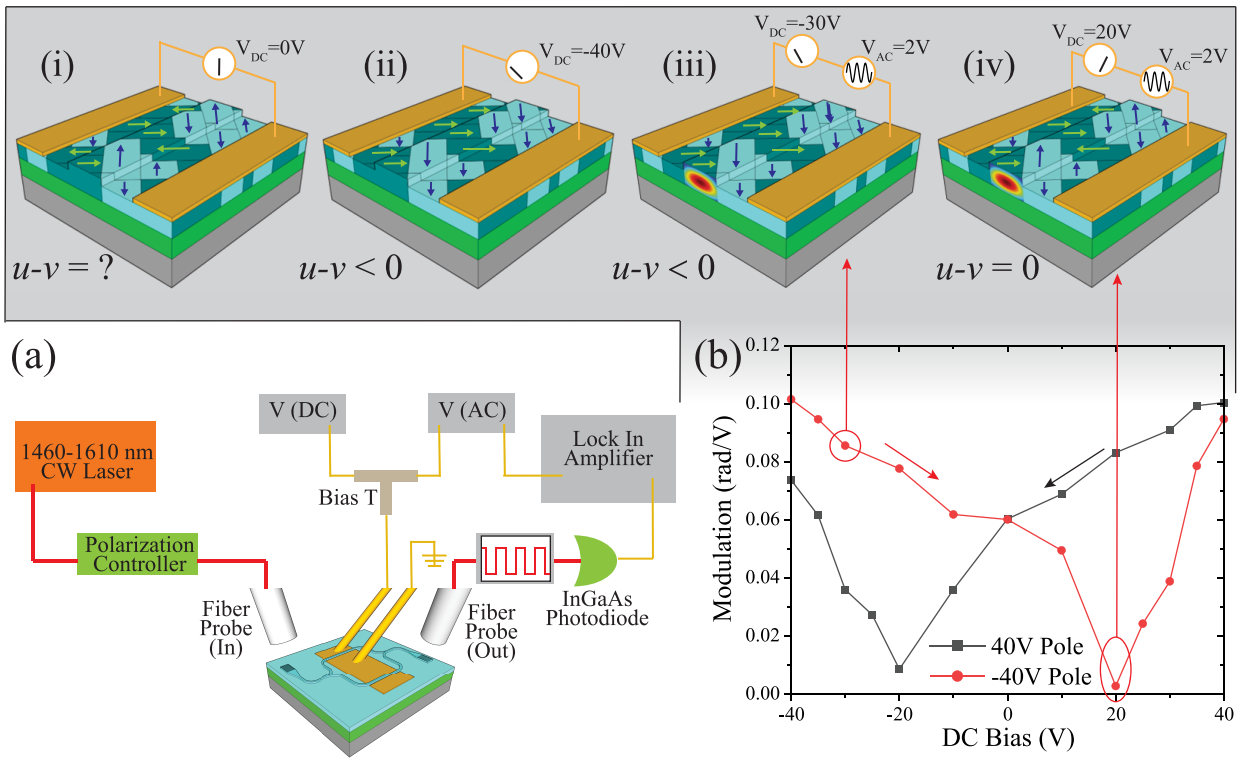

Figure 5. (a) Schematic of experimental setup for AC-modulated MZI characterization. (b) Experimental phase shift (in rad/V) of the AC-modulated MZI arm as a function of DC bias for poling at V_{pole} = −40 V (red) and V_{pole} = 40 V (black). Inset shows the schematic domain polarization of the BTO: (i) initial domain ratio is unknown, domain polarization is randomized ($u - v$ = ?). (ii) Under the application of a DC poling bias, the domains at least partially align ($u - v < 0$) and (iii) retain a net poling ($u - v < 0$) for voltages up to (iv) the coercive voltage V_c, at which point the net polarization of the domains is lost ($u - v \sim 0$).

coupling grating structure. Transmitted light is outcoupled via the second grating coupler and collected by a fiber positioned above the outcoupler, the output of which is focused into a Thorlabs PDA10CS photodiode. The photodiode signal is fed into a Zurich UHF lock-in amplifier (LIA). For the DC modulation experiment, a Keithley 2420 sourcemeter biases the device, and the laser is modulated by an Agilent 33210A function generator outputting square waves at 1017 Hz. The transmitted, modulated laser light is collected, and the signal is demodulated by the LIA, providing the relative transmission amplitude. In the AC modulation experiment, both AC and DC biases are applied to the device via a Fairview SB5792 bias-tee. The device is DC-biased and AC-modulated with a 419 kHz V_{pp} = 2 V sine wave from an Agilent 33210A function generator. The laser is run in continuous wave (CW) mode at the quadrature point closest to $\lambda_o \approx 1550$ nm for each DC bias. As the DC bias is shifted, the laser frequency is adjusted so that the device is operating at the quadrature point of the same interference fringe. The LIA is synchronized to the function generator and thus measures the amplitude modulation resulting from the AC bias. A detailed schematic of the setup used for the AC modulation experiment is shown in Figure 5a. Note that the devices studied in this work are not designed for the ultrahigh frequency operation recently demonstrated in BTO-based modulators,[44,45] largely a result of the capacitance associated with the devices' large-area electrodes (Supporting Information, section 3). While future work will look to investigate the ultimate limits of the monolithic BTO modulator bandwidth, here we use AC modulation to extract an effective Pockels coefficient and understand device domain poling. In both the DC and AC modulation experiments, bias is applied across one arm of the MZI, and the bias across the second arm is set to zero.

RESULTS AND DISCUSSION

In the DC modulation experiment, we first bias our device at −40 V for 60 min in order to pole the BTO (align the BTO domains with an applied electric field). The DC voltage is then scanned from −30 to 30 V in 10 V steps, with the MZI transmission spectra collected for each DC voltage by scanning the signal laser across the spectral range from λ_o = 1535−1565 nm and recording the LIA output at each wavelength. The resulting spectra are shown in Figure 4a,b. The near-perfect extinction of the transmitted signal at the transmission nulls indicates efficient 50/50 splitting and combining at our Y-splitters, as well as minimal waveguide loss in the unbalanced MZI (supported by the results from the cut-back measurement of the waveguide loss). The spectral spacing of the transmission maxima, for any applied bias, allows us to extract the group index of the optical mode in the waveguides, which we calculate from our experimental spectra to be $n_g \approx 2.5$, matching well with the group index determined by our numerical FDTD simulations. We observe a continuous blueshift in the MZI transmission spectra from applied biases of −30 to 20 V. However, from DC bias of 20 to 30 V we see a dramatic reversal (redshift) of the spectral tuning. We perform the same measurement but this time pole the BTO in the MZI arm using a 40 V DC bias for 60 min and scan the DC voltage from 30 to −30 V in −10 V steps. The resulting transmission spectra are shown in Figure 4c,d. We see a continuous blueshift

https://doi.org/10.1021/acsphotonics.3c01144
ACS Photonics XXXX, XXX, XXX−XXX

of the transmission spectra from 30 to −20 V, which again is reversed from −20 to −30 V.

To describe this phenomenon qualitatively, we first derive the effective index modulation of a single BTO domain polarized in the [001] direction under a low-frequency external electric field (Supporting Information, section 1). We can write the expression for the BTO refractive index, including the linear electro-optic effect, as

$$n_{ij}(E) = n_{ij}(0) - \frac{1}{2} n_{ij}^3(0) \sum_k r_{ijk} E_k \tag{1}$$

Next we can calculate the index modulation experienced by a TE mode (with an optical electric field polarized in the [011] direction) from a low-frequency external field in the [011] direction. Such a scenario matches both the low-frequency and optical electric fields of our device configuration (Figure 3a). Assuming an index modulation of $\Delta n_{[001]}(E) = +\Delta n_o(E)$ for this configuration, we can derive similar expressions for the BTO domains polarized in the $[00\bar{1}]$ $(-\Delta n_o(E))$, [010] $(+\Delta n_o(E))$ and $[0\bar{1}0]$ $(-\Delta n_o(E))$ directions, where the sign of the index modulation is determined by the domain orientation relative to the external field. The calculation of the net effective index modulation thus requires knowledge of the relative domain populations, which we write as $u - v$, where u is the fraction of domains polarized in the [001] and [010] directions and v represents the fractions of domains polarized in the $[00\bar{1}]$ and $[0\bar{1}0]$ directions. Simplifying the calculation process by leveraging domain symmetry[31,34,51] results in an expression for the net phase change of the fundamental TE mode propagating in an arm of the MZI:

$$\Delta\phi(E) = k_0 a \Delta n_{[001]}(u - v)L \tag{2}$$

where $k_0 = \omega/c$, L is the MZI arm length, and a (numerically determined to be 0.997) is the constant describing the relationship between the effective index of the optical mode and the BTO refractive index ($\Delta n_{eff} = a\Delta n_{BTO}$). Details of the derivation can be found in the Supporting Information.

When the BTO in the modulated arm of the MZI is initially poled with a DC bias of −40 V, we make the assumption that $u < v$ and thus $(u - v) < 0$. As the applied voltage increases (toward $V = 0$ V), the value of $|u - v|$ will decrease until, at the coercive field, $u - v = 0$. For these DC biases, $\Delta\phi$ will decrease in magnitude, resulting in a blueshift of the transmission spectrum. When the applied electric field is larger than the coercive field (≈20 V in our device), the value of $(u - v)$ will cross zero, and $\Delta\phi$ will flip sign and begin increasing in magnitude, accounting for the subsequent red-shifting of the transmission spectrum from 20 to 30 V. The same mechanism can also explain the transmission spectrum's behavior for the case when the BTO is first poled at 40 V and DC bias is decreased.

To extract the device's voltage-length product, we performed AC modulation experiments that effectively minimized effects of the low-frequency BTO domain dynamics on the electrically modulated BTO phase change. We first DC bias our device (−40 V), and we record the MZI transmission spectrum across the C-band. The signal laser, operating in CW mode, is tuned to a quadrature point at around 1550 nm. The device is driven with a 419 kHz sine wave, $V_{pp} = 2$ V, and the modulation amplitude of the transmitted intensity is measured by the LIA, and normalized to the device's transmission intensity at the quadrature point, resulting in an electrically modulated phase change per Volt. The DC bias is then stepped, and the process repeated. As shown in Figure 5b, when the DC offset was first set to −40 V and swept up to 40 V, the modulation amplitude drops to near zero at 20 V. Similar to the DC results shown in Figure 4, this suggests equivalent domain population ($u = v$) at $V_c = 20$ V, the voltage corresponding to the coercive field in the BTO waveguide. Similar results are obtained when the initial DC bias is 40 V and the DC bias stepped to −40 V. The inset in Figure 5b schematically shows the domain polarization process for the DC bias scan in the $+V$ direction. The initial sample is randomly polarized (Figure 5b-i), but upon application of a DC bias the sample becomes poled (Figure 5b-ii), such that $u - v < 0$. As the DC bias increases (toward $V = 0$ V), the domain polarization will decrease, but for fields far from the coercive field, $u - v < 0$, and modulation is still observed. However, when the applied field reaches the coercive field (in our device, at an applied bias $V_c = \pm 20$ V), the BTO is no longer polarized, and the effective index modulation disappears.

From eq 2, we expect to observe the largest modulation amplitude when the BTO plane is completely poled, in other words, when $|u - v| = 1$, under which conditions the effective Pockels coefficient can be extracted utilizing $r_{eff} = (\lambda_o g)/(a n_{BTO}^3 \Gamma' V_\pi L)$, where n_{BTO} is the refractive index of the BTO as measured by ellipsometry (Figure 1b), a is the proportionality constant relating Δn_{eff} and Δn_{BTO}, λ_o is the operating free-space wavelength (∼1550 nm), and g is the electrode spacing, which is 8 μm.[43] For hybrid devices, the expression for r_{eff} uses a Γ, which is the overlap integral of the optical mode with the BTO thin film. In our all-BTO devices, this term would be effectively unity. For the monolithic BTO waveguide, the appropriate weighting factor (Γ') is not the overlap of the optical mode with the BTO, but instead calculated from a weighted average of the DC electric field experienced by the optical mode (ie the average field seen by the optical mode, normalized to V/g). Though our monolithic devices offer strong modal overlap with the modulated BTO, our Γ' is not unity, as the DC electric field across the etched waveguide structure is not uniform. We calculate a $\Gamma' = 0.51$ from simulations of the optical and DC electric fields (Supporting Information, section 2).

For the experimental data in Figure 5 we would expect to observe a saturation in the modulation amplitude for DC bias amplitudes larger than the bias, resulting in $|u - v| \approx 1$. However, we do not observe such a saturation; instead the measured modulation amplitude appears to increase monotonically with increasing DC bias. Because of experimental limitations (maximum DC voltage of the bias-tee is ±40 V), the maximum measured value of the modulation amplitude, ∼0.1015 rad/V is likely much less than the maximum modulation amplitude achievable in our device. In fact, previous studies suggested that poling fields 3× larger than the fields used here were required to fully pole RF-sputtered BTO.[35] Nonetheless, we can calculate, using the value of the maximum phase shift achievable in our experimental setup, the voltage required to achieve a π phase shift in our MZI: $V_\pi = 30.94$ V. This corresponds to a (likely underestimated) voltage-length product of $V_\pi L = 2.32$ V·cm, from which we can extract an effective Pockels coefficient of $r_{eff} = 89$ pm/V.

The measured $V_\pi L$ of our MZI is competitive with state-of-the-art LN-based modulators, but somewhat higher than those of recently demonstrated hybrid BTO-based MZIs.[29,43,52] This is likely a result of the imperfect poling mentioned above, as

https://doi.org/10.1021/acsphotonics.3c01144
ACS Photonics XXXX, XXX, XXX−XXX

well as the lower effective Pockels coefficient of RF-sputtered BTO when compared to MBE-grown BTO. Further modifications can be implemented to improve our device performance to match, or exceed, that reported for hybrid BTO modulators.[35,43,46] First, the electrode spacing of our device (g = 8 μm) could be reduced somewhat without introducing additional losses in the waveguide (Supporting Information, section 4), with $V_\pi L$ scaling linearly with g. Previous work has suggested that r_{eff} increases linearly up to electric fields 3× those used in this work (after which r_{eff} saturates). The ability to fully pole these fields could bring our effective Pockels coefficient in line with that observed in previous work utilizing RF-sputtered BTO.[35] Alternatively, c-axis BTO waveguides, supporting TM waveguide modes, and incorporating a biasing configuration in the growth direction, could allow for a stronger effective linear electro-optic coefficient (r_{eff}) and larger electric fields.[46]

CONCLUSIONS

We have demonstrated monolithic BTO MZI modulators fabricated from RF-sputtered epitaxial BTO grown directly on silicon-on-insulator wafers. Our MZI components (coupling gratings, tapers, splitters, and waveguides) are all fabricated in BTO using e-beam lithography and ion milling, eschewing hybrid ridge or slot waveguide designs. The designed and fabricated waveguides comprising the all-BTO architecture are demonstrated to be low loss (3.17 dB/cm), compared to alternative hybrid architectures. The all-BTO architecture employed ensures a strong overlap of the optical mode with the modulated component of the nonlinear BTO. Fabricated MZIs were characterized under both DC and AC applied biases, and strong modulation of the MZI transmission was achieved in arm lengths of L = 750 μm. We qualitatively describe the voltage-dependent behavior of our MZIs by considering the domain polarization of the BTO in the modulated arm of the MZI. We extract a voltage-length product for our modulators of $V_\pi L$ = 2.32 V·cm, from which we can determine the effective Pockels coefficient of our BTO to be r_{eff} = 89 pm/V. Not only are our results competitive with state-of-the-art modulators leveraging the linear electro-optic effect, but we demonstrate this performance in an all-BTO architecture on Si (SOI) wafers, compatible with CMOS nanofabrication processes. The results presented here open the door to a new class of compact, low-power, CMOS-compatible, and BTO-based optoelectronic devices for silicon integrated photonics applications.

ASSOCIATED CONTENT

Supporting Information

The Supporting Information is available free of charge at https://pubs.acs.org/doi/10.1021/acsphotonics.3c01144.

Derivation of electrically modulated phase change; Calculating the overlap integral for monolithic BTO modulators; Estimation of device RF bandwidth; Effect of electrode gap size on BTO waveguide loss (PDF)

AUTHOR INFORMATION

Corresponding Author

Daniel M. Wasserman − *Department of Electrical and Computer Engineering, The University of Texas, Austin, Texas 78712, United States;* orcid.org/0000-0003-3234-0803; Email: dw@utexas.edu

Authors

Zuoming Dong − *Department of Electrical and Computer Engineering, The University of Texas, Austin, Texas 78712, United States;* orcid.org/0009-0006-8497-5754

Amogh Raju − *Department of Electrical and Computer Engineering, The University of Texas, Austin, Texas 78712, United States*

Agham B. Posadas − *Department of Physics, The University of Texas, Austin, Texas 78712, United States*

Marc Reynaud − *Department of Physics, The University of Texas, Austin, Texas 78712, United States*

Alexander A. Demkov − *Department of Physics, The University of Texas, Austin, Texas 78712, United States;* orcid.org/0000-0003-4241-3519

Complete contact information is available at: https://pubs.acs.org/10.1021/acsphotonics.3c01144

Funding

This research was supported by a Multidisciplinary University Research Initiative from the Air Force Office of Scientific Research (AFOSR MURI Award No. FA9550-22-1-0307).

Notes

The authors declare no competing financial interest.

REFERENCES

(1) Reed, G. T.; Mashanovich, G. Z.; Gardes, F. Y.; Nedeljkovic, M.; Hu, Y.; Thomson, D. J.; Li, K.; Wilson, P. R.; Chen, S.-W.; Hsu, S. S. Recent breakthroughs in carrier depletion based silicon optical modulators. *Nanophotonics* **2014**, *3*, 229−245.

(2) Wooten, E. L.; Kissa, K. M.; Yi-Yan, A.; Murphy, E. J.; Lafaw, D. A.; Hallemeier, P. F.; Maack, D.; Attanasio, D. V.; Fritz, D. J.; McBrien, G. J.; Bossi, D. A review of lithium niobate modulators for fiber-optic communications systems. *IEEE J. Sel. Top. Quantum Electron.* **2000**, *6*, 69−82.

(3) Mercante, A. J.; Shi, S.; Yao, P.; Xie, L.; Weikle, R. M.; Prather, D. W. Thin film lithium niobate electro-optic modulator with terahertz operating bandwidth. *Opt. Express* **2018**, *26*, 14810−14816.

(4) Van Acoleyen, K.; Bogaerts, W.; Jágerská, J.; Le Thomas, N.; Houdré, R.; Baets, R. Off-chip beam steering with a one-dimensional optical phased array on silicon-on-insulator. *Opt. Lett.* **2009**, *34*, 1477−1479.

(5) Van Acoleyen, K.; Rogier, H.; Baets, R. Two-dimensional optical phased array antenna on silicon-on-insulator. *Opt. Express* **2010**, *18*, 13655−13660.

(6) Sun, J.; Timurdogan, E.; Yaacobi, A.; Hosseini, E. S.; Watts, M. R. Large-scale nanophotonic phased array. *Nature* **2013**, *493*, 195−199.

(7) Jones, D. J.; Diddams, S. A.; Ranka, J. K.; Stentz, A.; Windeler, R. S.; Hall, J. L.; Cundiff, S. T. Carrier-envelope phase control of femtosecond mode-locked lasers and direct optical frequency synthesis. *Science* **2000**, *288*, 635−639.

(8) Fortier, T.; Roos, P.; Jones, D.; Cundiff, S. T.; Bhat, R.; Sipe, J. E. Carrier-envelope phase-controlled quantum interference of injected photocurrents in semiconductors. *Phys. Rev. Lett.* **2004**, *92*, 147403.

(9) Giorgetta, F. R.; Swann, W. C.; Sinclair, L. C.; Baumann, E.; Coddington, I.; Newbury, N. R. Optical two-way time and frequency transfer over free space. *Nat. Photonics* **2013**, *7*, 434−438.

(10) Cocorullo, G.; Rendina, I. Thermo-optical modulation at 1.5 μm in silicon etalon. *Electron. Lett.* **1992**, *28*, 83−85.

(11) Espinola, R.; Tsai, M.; Yardley, J. T.; Osgood, R. Fast and low-power thermooptic switch on thin silicon-on-insulator. *IEEE Photonics Technology Letters* **2003**, *15*, 1366−1368.

(12) Gu, L.; Jiang, W.; Chen, X.; Chen, R. T. Thermooptically tuned photonic crystal waveguide silicon-on-insulator Mach−Zehnder interferometers. *IEEE Photonics Technology Letters* **2007**, *19*, 342−344.

(13) Liu, A.; Jones, R.; Liao, L.; Samara-Rubio, D.; Rubin, D.; Cohen, O.; Nicolaescu, R.; Paniccia, M. A high-speed silicon optical modulator based on a metal−oxide−semiconductor capacitor. *Nature* **2004**, *427*, 615−618.
(14) Xu, Q.; Manipatruni, S.; Schmidt, B.; Shakya, J.; Lipson, M. 12.5 Gbit/s carrier-injection-based silicon micro-ring silicon modulators. *Opt. Express* **2007**, *15*, 430−436.
(15) Marris-Morini, D.; Vivien, L.; Fédéli, J. M.; Cassan, E.; Lyan, P.; Laval, S. Low loss and high speed silicon optical modulator based on a lateral carrier depletion structure. *Opt. Express* **2008**, *16*, 334−339.
(16) De, S.; Das, R.; Varshney, R. K.; Schneider, T. Design and Simulation of Thermo-Optic Phase Shifters With Low Thermal Crosstalk for Dense Photonic Integration. *IEEE Access* **2020**, *8*, 141632−141640.
(17) Thomaschewski, M.; Bozhevolnyi, S. I. Pockels modulation in integrated nanophotonics. *Applied Physics Reviews* **2022**, *9*, 021311.
(18) Zhang, M.; Wang, C.; Chen, X.; Bertrand, M.; Shams-Ansari, A.; Chandrasekhar, S.; Winzer, P.; Lončar, M. *Ultra-high bandwidth integrated lithium niobate modulators with record-low Vπ. 2018 Optical Fiber Communications Conference and Exposition*; OFC, 2018; pp 1−3.
(19) Poberaj, G.; Hu, H.; Sohler, W.; Guenter, P. Lithium niobate on insulator (LNOI) for micro-photonic devices. *Laser & Photonics Reviews* **2012**, *6*, 488−503.
(20) Wang, C.; Zhang, M.; Chen, X.; Bertrand, M.; Shams-Ansari, A.; Chandrasekhar, S.; Winzer, P.; Lončar, M. Integrated lithium niobate electro-optic modulators operating at CMOS-compatible voltages. *Nature* **2018**, *562*, 101−104.
(21) Jazbinšek, M.; Zgonik, M. Material tensor parameters of $LiNbO_3$ relevant for electro-and elasto-optics. *Appl. Phys. B: Laser Opt.* **2002**, *74*, 407−414.
(22) Brinkmann, R.; Baumann, I.; Dinand, M.; Sohler, W.; Suche, H. Erbium-doped single- and double-pass Ti:$LiNbO_3$ waveguide amplifiers. *IEEE J. Quantum Electron.* **1994**, *30*, 2356−2360.
(23) Tanzilli, S.; De Riedmatten, H. D.; Tittel, W.; Zbinden, H.; Baldi, P.; De Micheli, M. D.; Ostrowsky, D.; Gisin, N. Highly efficient photon-pair source using periodically poled lithium niobate waveguide. *Electron. Lett.* **2001**, *37* (2), 26−28.
(24) Miller, G. D.; Batchko, R. G.; Tulloch, W. M.; Weise, D. R.; Fejer, M. M.; Byer, R. L. 42%-efficient single-pass CW second-harmonic generation in periodically poled lithium niobate. *Opt. Lett.* **1997**, *22*, 1834−1836.
(25) Rabiei, P.; Ma, J.; Khan, S.; Chiles, J.; Fathpour, S. Heterogeneous lithium niobate photonics on silicon substrates. *Opt. Express* **2013**, *21*, 25573−25581.
(26) He, M.; Xu, M.; Ren, Y.; Jian, J.; Ruan, Z.; Xu, Y.; Gao, S.; Sun, S.; Wen, X.; Zhou, L.; Liu, L.; Guo, C.; Chen, H.; Yu, S.; Liu, L.; Cai, X. High-performance hybrid silicon and lithium niobate Mach−Zehnder modulators for 100 Gbit s- 1 and beyond. *Nat. Photonics* **2019**, *13*, 359−364.
(27) Liu, Y.; Li, H.; Liu, J.; Tan, S.; Lu, Q.; Guo, W. Low V π thin-film lithium niobate modulator fabricated with photolithography. *Opt. Express* **2021**, *29*, 6320−6329.
(28) Jin, M.; Chen, J.; Sua, Y.; Kumar, P.; Huang, Y. Efficient electro-optical modulation on thin-film lithium niobate. *Opt. Lett.* **2021**, *46*, 1884−1887.
(29) Xiong, C.; Pernice, W. H.; Ngai, J. H.; Reiner, J. W.; Kumah, D.; Walker, F. J.; Ahn, C. H.; Tang, H. X. Active silicon integrated nanophotonics: ferroelectric $BaTiO_3$ devices. *Nano Lett.* **2014**, *14*, 1419−1425.
(30) Wang, T.-J.; Chu, C.-H.; Lin, C.-Y. Electro-optically tunable microring resonators on lithium niobate. *Opt. Lett.* **2007**, *32*, 2777−2779.
(31) Abel, S.; Eltes, F.; Ortmann, J. E.; Messner, A.; Castera, P.; Wagner, T.; Urbonas, D.; Rosa, A.; Gutierrez, A. M.; Tulli, D.; Ma, P.; Baeuerle, B.; Josten, A.; Heni, W.; Caimi, D.; Czornomaz, L.; Demkov, A.; Leuthold, J.; Sanchis, P.; Fompeyrine, J. Large Pockels effect in micro-and nanostructured barium titanate integrated on silicon. *Nat. Mater.* **2019**, *18*, 42−47.
(32) Bernasconi, P.; Zgonik, M.; Günter, P. Temperature dependence and dispersion of electro-optic and elasto-optic effect in perovskite crystals. *J. Appl. Phys.* **1995**, *78*, 2651−2658.
(33) Abel, S.; Stöferle, T.; Marchiori, C.; Caimi, D.; Czornomaz, L.; Stuckelberger, M.; Sousa, M.; Offrein, B. J.; Fompeyrine, J. A hybrid barium titanate−silicon photonics platform for ultraefficient electro-optic tuning. *Journal of Lightwave Technology* **2016**, *34*, 1688−1693.
(34) Abel, S.; Stöferle, T.; Marchiori, C.; Rossel, C.; Rossell, M. D.; Erni, R.; Caimi, D.; Sousa, M.; Chelnokov, A.; Offrein, B. J.; Fompeyrine, J. A strong electro-optically active lead-free ferroelectric integrated on silicon. *Nat. Commun.* **2013**, *4*, 1671.
(35) Posadas, A. B.; Park, H.; Reynaud, M.; Cao, W.; Reynolds, J. D.; Guo, W.; Jeyaselvan, V.; Beskin, I.; Mashanovich, G. Z.; Warner, J. H.; Demkov, A. A. Thick $BaTiO_3$ Epitaxial Films Integrated on Si by RF Sputtering for Electro-Optic Modulators in Si Photonics. *ACS Appl. Mater. Interfaces* **2021**, *13*, 51230−51244.
(36) Lin, W.; Tseng, T.-Y.; Lu, H.; Tu, S.; Yang, S.; Lin, I. Growth and ferroelectricity of epitaxial-like $BaTiO_3$ films on single-crystal MgO, $SrTiO_3$, and silicon substrates synthesized by pulsed laser deposition. *J. Appl. Phys.* **1995**, *77*, 6466−6471.
(37) Gill, D.; Conrad, C.; Ford, G.; Wessels, B.; Ho, S. Thin-film channel waveguide electro-optic modulator in epitaxial $BaTiO_3$. *Appl. Phys. Lett.* **1997**, *71*, 1783−1785.
(38) Gill, D. M.; Conrad, C. W.; Ford, G.; Wessels, B. W.; Ho, S. T. Thin-film channel waveguide electro-optic modulator in epitaxial $BaTiO_3$. *Appl. Phys. Lett.* **1997**, *71*, 1783−1785.
(39) Hiltunen, J.; Seneviratne, D.; Sun, R.; Stolfi, M.; Tuller, H. L.; Lappalainen, J.; Lantto, V. $BaTiO_3$−$SrTiO_3$ multilayer thin film electro-optic waveguide modulator. *Appl. Phys. Lett.* **2006**, *89*, 242904.
(40) Jin, T.; Li, L.; Zhang, B.; Lin, H.-Y. G.; Wang, H.; Lin, P. T. Monolithic mid-infrared integrated photonics using silicon-on-epitaxial barium titanate thin films. *ACS Appl. Mater. Interfaces* **2017**, *9*, 21848−21855.
(41) Jin, T.; Lin, P. T. Efficient mid-infrared electro-optical waveguide modulators using ferroelectric barium titanate. *IEEE J. Sel. Top. Quantum Electron.* **2020**, *26*, 1−7.
(42) Ortmann, J. E.; Eltes, F.; Caimi, D.; Meier, N.; Demkov, A. A.; Czornomaz, L.; Fompeyrine, J.; Abel, S. Ultra-low-power tuning in hybrid barium titanate−silicon nitride electro-optic devices on silicon. *ACS Photonics* **2019**, *6*, 2677−2684.
(43) Eltes, F.; Mai, C.; Caimi, D.; Kroh, M.; Popoff, Y.; Winzer, G.; Petousi, D.; Lischke, S.; Ortmann, J. E.; Czornomaz, L.; Zimmermann, L.; Fompeyrine, J.; Abel, S. A $BaTiO_3$-based electro-optic Pockels modulator monolithically integrated on an advanced silicon photonics platform. *Journal of Lightwave Technology* **2019**, *37*, 1456−1462.
(44) Chelladurai, D.; Kohli, M.; Horst, Y.; Winiger, J.; Moor, D.; Blatter, T.; Kulmer, L.; Eppenberger, M.; Messner, A.; Convertino, C.; Eltes, F.; Fedoryshyn, Y.; Leuthold, J. *Pockels coefficients in thin-film barium titanate and lithium niobate up to 300 GHz*; CLEO: Science and Innovations, 2023; p SM2H-8.
(45) Chelladurai, D.; Kohli, M.; Horst, Y.; Eppenberger, M.; Kulmer, L.; Blatter, T.; Winiger, J.; Moor, D.; Messner, A.; Convertino, C.; Eltes, F.; Fedoryshyn, Y.; Leuthold, J. Electro-Optic Frequency Response of Thin-Film Barium Titanate (BTO) from 20 to 270 GHz. European Conference and Exhibition on Optical Communication 2022, Basel, Switzerland, 18−22 September, 2022; Optica Publishing Group. 2022; paper We5.72.
(46) Posadas, A. B.; Stenger, V. E.; DeFouw, J. D.; Warner, J. H.; Demkov, A. A. RF-sputtered Z-cut electro-optic barium titanate modulator on silicon photonic platform. *J. Appl. Phys.* **2023**, *134*, 073101.
(47) Rahim, A.; Hermans, A.; Wohlfeil, B.; Petousi, D.; Kuyken, B.; Van Thourhout, D. V.; Baets, R. G. Taking silicon photonics modulators to a higher performance level: state-of-the-art and a review of new technologies. *Advanced Photonics* **2021**, *3*, 024003.
(48) Mazet, L.; Yang, S. M.; Kalinin, S. V.; Schamm-Chardon, S.; Dubourdieu, C. A review of molecular beam epitaxy of ferroelectric

https://doi.org/10.1021/acsphotonics.3c01144
ACS Photonics XXXX, XXX, XXX−XXX

BaTiO3 films on Si, Ge and GaAs substrates and their applications. *Sci. Technol. Adv. Mater.* **2015**, *16*, 036005.
(49) Ortmann, J. E.; McCartney, M. R.; Posadas, A.; Smith, D. J.; Demkov, A. A. Epitaxial oxides on glass: a platform for integrated oxide devices. *ACS Applied Nano Materials* **2019**, *2*, 7713−7718.
(50) Vasudevan, A. T.; Selvaraja, S. K. Domain effects on the electro-optic properties of thin-film barium titanate. *Opt. Mater. Express* **2023**, *13*, 956−965.
(51) Messner, A.; Eltes, F.; Ma, P.; Abel, S.; Baeuerle, B.; Josten, A.; Heni, W.; Caimi, D.; Fompeyrine, J.; Leuthold, J. Plasmonic ferroelectric modulators. *Journal of Lightwave Technology* **2019**, *37*, 281−290.
(52) Posadas, A.; Stenger, V.; DeFouw, J.; Mashanovich, G.; Wasserman, D.; Demkov, A. Electro-Optic Barium Titanate Modulators on Silicon Photonics Platform, 2023. IEEE Silicon Photonics Conference (SiPhotonics), Orlando, Florida, 12−16 November, 2023, IEEE, 2023; pp 1−2.

https://doi.org/10.1021/acsphotonics.3c01144
ACS Photonics XXXX, XXX, XXX−XXX